

Optimal statistic for detecting gravitational wave signals from binary inspirals with LISA

Aaron Rogan and Sukanta Bose

Department of Physics and Program of Astronomy, Washington State University,
Pullman, WA 99164-2814, USA

E-mail: roganelli@wsu.edu, sukanta@wsu.edu

PACS numbers: 04.80.Nn, 95.55.Ym, 95.75.Pq, 07.05.Kf, 97.80.-d, 97.60.Jd

Abstract. A binary compact object early in its inspiral phase will be picked up by its nearly monochromatic gravitational radiation by LISA. But even this innocuous appearing candidate poses interesting detection challenges. The data that will be scanned for such sources will be a set of three functions of LISA's twelve data streams obtained through time-delay interferometry, which is necessary to cancel the noise contributions from laser-frequency fluctuations and optical-bench motions to these data streams. We call these three functions pseudo-detectors. The sensitivity of any pseudo-detector to a given sky position is a function of LISA's orbital position. Moreover, at a given point in LISA's orbit, each pseudo-detector has a different sensitivity to the same sky position. In this work, we obtain the optimal statistic for detecting gravitational wave signals, such as from compact binaries early in their inspiral stage, in LISA data. We also present how the sensitivity of LISA, defined by this optimal statistic, varies as a function of sky position and LISA's orbital location. Finally, we show how a real-time search for inspiral signals can be implemented on the LISA data by constructing a bank of templates in the sky positions.

1. Introduction

The commissioning of Earth-based long-baseline gravitational wave (GW) interferometers has finally come to fruition a little less than three decades since the discovery of the Hulse and Taylor binary pulsar in 1974 [1] and the subsequent confirmation of the emission of gravitational waves (GWs) by that system.[2] On the other hand, the Laser Interferometric Space Antenna (LISA) is being designed as a space-based detector to observe low-frequency GWs (in the milli- to deci-hertz band) to complement the high-frequency observations (in the deca- to kilo-hertz band) of its Earth-based counterparts. Many of the sources of low-frequency GWs fall in the category of compact binary objects, which include white dwarfs, neutron stars, and black holes. During the early stages of the inspiral, these compact binaries will emit almost monochromatic low-frequency gravitational waves, which will produce detectable signals in the LISA data.

LISA will comprise three spacecrafts located at the vertices of a nearly equilateral triangle (as shown in Fig. 1) with the side lengths equal to 5 million kilometers.[3] Each craft will house a couple of laser-mounted optical benches and proof masses and will freely fall around the Sun in an orbit that lies on a plane slightly tilted with respect to the ecliptic. The tilt will vary from one craft to the other. By inclining the plane of the triangle to the ecliptic by a constant angle of 60° , the side-length of the triangle can be maintained at a fixed value. In the process, the triangle will complete one spin about its normal while its centroid, trailing behind the Earth by about 8.3 million kilometers, completes one orbit around the Sun.

The effect of a GW on LISA will be to change the physical distances between its freely falling proof masses. This change will be registered as fractional frequency shifts in the six laser beams exchanged among the three space-crafts. The shifts will have additional contributions from various noise sources. These include two primary ones, namely, the laser-frequency fluctuations (contributing a fractional shift of about $10^{-13} \text{ Hz}^{-1/2}$) and the optical-bench motions (with a fractional shift of about $10^{-16} \text{ Hz}^{-1/2}$). In order to detect the GWs (with a strain around $10^{-21} \text{ Hz}^{-1/2}$), it is imperative that these noises be mitigated by several orders of magnitude. A data analysis technique for achieving this goal was accomplished by Armstrong, Estabrook, and Tinto.[4]. They showed that by combining appropriately the time-delayed versions of these six data streams, with six additional ones arising from laser beam exchanges between adjacent optical benches on each craft, one can eliminate the two primary noises, thus, rendering the LISA data analyzable for GW signals.

In this paper, we formulate a strategy for detecting nearly monochromatic gravitational waves from inspiraling compact binary objects in the LISA data. There are two complementary aspects to such a strategy. The first is to deduce the maximum number of noise-independent detectors that LISA offers. And the second is to construct the appearance of a GW signal in them. This allows one to match the data from these detectors with a template of the expected signal in them. Whether a match is strong enough to warrant a detection is then decided based on the rate of false alarms

at the level of that match. For the problem of detecting low-mass compact binaries, involving white-dwarfs and neutron stars, the waveforms obtained by the quadrupole approximation [5] suffice for accurately modeling the expected signal. This waveform allows for a slightly “chirping” source, i.e., a source whose orbital frequency Ω_0 is increasing at a rate $\dot{\Omega}_0 \ll \Omega_0/T$, where T is the observation period. We will use this waveform as a template in our detection strategy.

The layout of the paper is as follows. In Sec. 2, we enunciate the three noise-independent data combinations, or “pseudo-detectors”, that were first obtained in Ref. [6] by combining the frequency shifts of the twelve data streams exchanged among the LISA spacecrafts through time-delay interferometry (TDI) [7]. In Sec. 3, we obtain the form of the gravitational-wave strain caused by a compact binary source in these three pseudo-detectors. This provides the templates required to search for signals from such sources in the LISA data. We then study the antenna patterns of these pseudo-detectors at different points in LISA’s orbit, emphasizing how their relative sensitivities to a mildly chirping source vary as a function of sky position and source frequency. The study bears out the fact that noise-independence of detectors is a property distinct from their geometric independence. Indeed, at GW wavelengths larger than about 0.1 AU, which we will term as the long-wavelength limit, the strain of the third pseudo-detector tends to the difference of the strain of the first two. We then derive the optimal statistic for detecting gravitational waves from (non-spinning) compact binary inspirals by coherently combining the data of the three pseudo-detectors in Sec. 4.

The statistic obtained here tracks the Doppler modulation of the source frequency induced by the motion and time-varying orientation of LISA with respect to that source.[9] For Gaussian noise, we derive the probability distribution of our statistic, which can be used to compute the signal-to-noise ratio (SNR) of a candidate event. We use this distribution to predict the behavior of false-alarm and detection rates as a function of the detection threshold set for the statistic. In Sec. 5, we construct the metric on the space of parameters that allows one to estimate the fractional loss of SNR for a given mismatch between the template and the signal parameters. Using this metric we estimate the number of templates that will be required to search the full astrophysically relevant volume of the parameter space while suffering a loss in SNR of no more than 3%. We also estimate the computational speed required to implement such a search in real time. We briefly summarize the results obtained in Sec. 6, especially, stressing the applicability of our formalism to searches in the recently found second-generation TDI data combinations.[11, 12, 13] Note that in the expressions appearing in this paper, we set the gravitational coupling constant (G) and the speed of light (c) to unity.

2. The pseudo-detectors

As illustrated in Fig. 1, LISA consists of three spacecrafts, labeled $i = 1, 2$, and 3, located clockwise at the correspondingly labeled vertices of an almost equilateral triangle. Let the arm-lengths of this triangle be L_1 , L_2 , and L_3 , such that L_i is the length of the arm

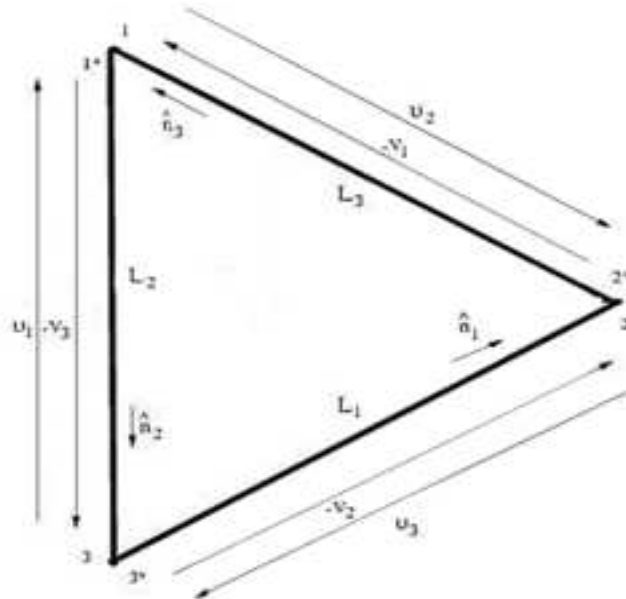


Figure 1. LISA consists of 3 spacecrafts located at the vertices of an equilateral triangle. These craft exchange six elementary data streams, labeled U_i and $-V_i$. The U_i beams propagate clockwise, whereas the $-V_i$ propagate counterclockwise.

facing the vertex i . For specifying the orientation of each arm, we assign unit vectors $\hat{\mathbf{n}}_i$ along them, such that their directions are oriented anticlockwise about the triangle. Each spacecraft will have two optical benches (denoted by i and i^* in Fig. 1) equipped with independent lasers and photodetectors. Thus, each spacecraft will shoot two beams towards the other two spacecrafts, respectively, resulting in six one-way beams along the 3 arms.

The effect of an impinging GW is to cause a shift in the frequency of the laser beams. But a GW is not the only source causing such a shift. The laser-frequency fluctuation is another source. If ν_0 is the central frequency of all the lasers in LISA, then the fractional shift caused by such fluctuations in the beam originating at optical bench i is

$$C_i(t) \equiv \frac{\Delta\nu_i(t)}{\nu_0} . \quad (1)$$

Similarly for the beam from the bench i^* . What is measured, however, is the frequency fluctuation in the beam from one bench relative to that in the beam from a bench in

one of the two other vertices. This way one obtains three “clockwise” oriented streams, U_i , and three “anticlockwise” oriented streams, $-V_i$. The frequency fluctuation in the beam from bench $(i - 1)$ relative to that in the beam originating at bench i^* is termed U_i . ‡ Therefore, $U_1(t) \equiv C_3(t - L_2) - C_1(t)$ is the data stream measured by beating the beam transmitted by bench 3 against that of bench 1^* , measured at time t at bench 1. The remaining two streams, namely, U_2 and U_3 , can be obtained by cyclic permutation of the indices in the U_1 expression. (Thus, $U_2(t) \equiv C_1(t - L_3) - C_2(t)$, and so on.) Three more data streams, termed $-V_i$, are obtained by measuring the frequency fluctuation in the beam from bench $(i + 1)^*$ relative to that originating at bench i . For instance, $-V_1(t) \equiv C_2(t - L_3) - C_1(t)$. Once again, the remaining two $-V_i$ streams can be obtained by cyclic permutation of the indices in the above expression for $-V_1$. (Hence, $-V_2(t) \equiv C_3(t - L_1) - C_2(t)$, and so on.)

The fractional shift $C_3(t - L_2)$ is constructed from $C_3(t)$ by shifting back the latter stream in time by an amount L_2 . For brevity of expressions, we introduce the time-shift operator ζ_i by its action on a data stream $x(t)$ as in:

$$\zeta_i x(t) = x(t - L_i) \quad , \quad (2)$$

where the label i denotes the arm along which the time-shift is affected. One can thus define the 6 inter-craft streams as follows[14]:

$$\begin{aligned} U_1 &= \zeta_2 C_3 - C_1, & U_2 &= \zeta_3 C_1 - C_2, & U_3 &= \zeta_1 C_2 - C_3, \\ V_1 &= C_1 - \zeta_3 C_2, & V_2 &= C_2 - \zeta_1 C_3, & V_3 &= C_3 - \zeta_2 C_1. \end{aligned} \quad (3)$$

Note that the effect of such a shift on the Fourier components, $\tilde{x}(f) \equiv \int_{-\infty}^{\infty} x(t) e^{2\pi i f t} dt$, of the data is to change them to $e^{-2\pi i f L_i} \tilde{x}(f)$, where f is a frequency variable. Therefore, the effect of the operator $\prod_{i=1}^3 \zeta_i^{\alpha_i}$ on a data stream is to change its Fourier transform by the factor $e^{-2\pi i f \sum_{i=1}^3 \alpha_i L_i}$.

These data streams, however, are expected to suffer from several noise sources, two of which, viz., the laser-frequency fluctuations and the optical-bench motions, tower over the others. The two other noise sources are the photon-shot noise and the fluctuations in the motion of the proof masses. The laser-frequency fluctuations directly influence the fractional frequency-shifts, C_i , and, therefore, the data streams U_i and V_i . The effect of the optical bench motions on the C_i is additive: Let the random velocities of the optical benches be \mathbf{v}_i and \mathbf{v}_{i^*} . This causes a Doppler shift in the frequency of the lasers mounted on those benches, which in turn modifies the C_i to

$$\begin{aligned} C_1 &\rightarrow C_1 - \hat{\mathbf{n}}_3 \cdot \mathbf{v}_1, \\ C_{1^*} &\rightarrow C_{1^*} + \hat{\mathbf{n}}_2 \cdot \mathbf{v}_{1^*}. \end{aligned} \quad (4)$$

The remaining C_i and C_{i^*} can be inferred by cyclically permuting the indices in the above expression. If \mathbf{u}_{i,i^*} are the random velocities of the proof masses on benches i and

‡ Note that the indices i and $i \pm 1$ can take only 1, 2, and 3 as values. These three numbers are ordered clockwise in Fig. 1. By convention, whereas $i + 1$ equals the number next to i while going clockwise in that figure, $i - 1$ equals the number preceding i . E.g., when $i = 3$, we take $i - 1 = 2$ and $i + 1 = 1$; when $i = 1$, we take $i - 1 = 3$ and $i + 1 = 2$.

i^* , then it is easy to see that the value of U_1 and V_1 gets affected by additional terms $2\hat{\mathbf{n}}_2 \cdot \mathbf{u}_{1^*}$ and $2\hat{\mathbf{n}}_3 \cdot \mathbf{u}_1$, respectively. Finally, when there is a GW signal present, these streams will receive additional contribution owing to the fractional frequency shifts caused by it. Thus, in the presence of the above noise sources and signal, the data streams get modified as

$$\begin{aligned} U_1 &\rightarrow U_1 = \zeta_2(C_3 - \hat{\mathbf{n}}_2 \cdot \mathbf{v}_3) - (C_{1^*} + \hat{\mathbf{n}}_2 \cdot \mathbf{v}_{1^*}) + 2\hat{\mathbf{n}}_2 \cdot \mathbf{u}_{1^*} + n_{U_1}^{\text{shot}} + U_1^{\text{GW}} \quad , \\ V_1 &\rightarrow V_1 = -\zeta_3(C_{2^*} + \hat{\mathbf{n}}_3 \cdot \mathbf{v}_{2^*}) + (C_1 - \hat{\mathbf{n}}_3 \cdot \mathbf{v}_1) + 2\hat{\mathbf{n}}_3 \cdot \mathbf{u}_1 - n_{V_1}^{\text{shot}} - V_1^{\text{GW}} \quad (5) \end{aligned}$$

where $n_{U_i, V_i}^{\text{shot}}$ are the photon-shot noises and U_i^{GW} and V_i^{GW} are the GW signals present in the U_i and V_i data streams, respectively. The four remaining U_i and V_i streams can be obtained from the above expressions by cyclic permutations of the indices. In the rest of the paper the U_i and V_i will refer to these modified streams. When a (GW) signal is absent, they will still be given by these modified expression, but with $U_i^{\text{GW}} = 0$ and $V_i^{\text{GW}} = 0$. The form of U_i^{GW} and V_i^{GW} in the presence of a signal will be explored in the next section.

In addition to the six inter-craft data streams discussed above there is supplementary information available about the noise sources in the intra-craft beams exchanged through the optical fibers connecting two adjacent optical benches i and i^* located in the i th craft. In all there are six intra-craft beams, two per bench pair. But the two intra-craft beams within a craft can be beaten against each other to produce a single stream that is directly relevant to noise suppression. To wit, at craft 1, by beating the frequency of the beam from bench 1 relative to that on bench 1^* , one forms the stream,

$$W_1 = (C_1 - \hat{\mathbf{n}}_3 \cdot \mathbf{v}_1) - (C_{1^*} + \hat{\mathbf{n}}_2 \cdot \mathbf{v}_{1^*}) + \hat{\mathbf{n}}_3 \cdot \mathbf{u}_1 + \hat{\mathbf{n}}_2 \cdot \mathbf{u}_{1^*} \quad . \quad (6)$$

Two other intra-craft data combinations, W_2 and W_3 , can be obtained by the cyclic permutation of indices in the above expression. Note that these intra-craft streams will bear negligible influence from any impinging gravitational wave. Nevertheless, as we explain below, they offer information on laser-frequency fluctuations and optical-bench motions that can be used to render the U_i and V_i streams essentially free of any noise from these two sources. Together with the U_i and V_i , the W_i form a total of nine data streams that a data analyst has recourse to in hunting for a GW signal in LISA.

Following the work of Tinto and Armstrong [7], it was shown by Dhurandhar et al. [14] that by acting on the 6 inter-craft streams, U_i , V_i , and the 3 intra-craft streams, W_i , with certain polynomials, p_i^A , q_i^A , and r_i^A , of the time-shift operators, ζ_i , one can form several combinations of time-delayed data streams,

$$x^A(t) = \sum_{i=1}^3 [p_i^A V_i(t) + q_i^A U_i(t) + r_i^A W_i(t)] \quad , \quad (7)$$

that have the laser-frequency and the optical-bench motion noise eliminated. Above, A labels the different combinations so obtained. The above technique of constructing

such data combinations of pseudo-detectors is called time-delay interferometry. The pseudo-detectors can be recast as

$$x^A = \text{Trace} [\mathbf{e}^A \cdot \mathbf{Z}] \quad , \quad (8)$$

where

$$\mathbf{e}^A = \begin{pmatrix} p_1^A & p_2^A & p_3^A \\ q_1^A & q_2^A & q_3^A \\ r_1^A & r_2^A & r_3^A \end{pmatrix} \quad \text{and} \quad \mathbf{Z} = \begin{pmatrix} V_1 & U_1 & W_1 \\ V_2 & U_2 & W_2 \\ V_3 & U_3 & W_3 \end{pmatrix} . \quad (9)$$

Thus, for a given choice of the data streams U_i, V_i, W_i (and, therefore, the matrix \mathbf{Z}), the matrix \mathbf{e}^A of the time-shift polynomials forms a representation of the pseudo-detectors x^A .

Of the several possible pseudo-detectors, only 3 are linearly independent and have a non-vanishing GW strain in them, in general [6, 15]. The three that will be discussed here are defined by their corresponding \mathbf{e}^A :

$$\mathbf{e}^1 = \begin{pmatrix} 1 - \zeta & 1 + 2\zeta & -2 - \zeta \\ 1 + 2\zeta & 1 - \zeta & -2 - \zeta \\ \zeta^2 - 1 & \zeta^2 - 1 & 2(1 - \zeta^2) \end{pmatrix} , \quad \mathbf{e}^2 = \begin{pmatrix} -\zeta - 1 & 1 & \zeta \\ -1 & 1 + \zeta & -\zeta \\ 1 - \zeta^2 & -1 + \zeta^2 & 0 \end{pmatrix} , \quad (10)$$

and

$$\mathbf{e}^3 = \begin{pmatrix} 1 & 1 & 1 \\ 1 & 1 & 1 \\ -1 - \zeta & -1 - \zeta & -1 - \zeta \end{pmatrix} . \quad (11)$$

In the above expressions, it is assumed that all arm lengths are almost identical. Therefore, $\zeta_1 \simeq \zeta_2 \simeq \zeta_3 \equiv \zeta$. It is important to note that these data combinations diagonalize their noise covariance matrix [16] and, therefore, are also noise-independent.

Although the laser-frequency noise is eliminated in the $x^A(t)$, there is still present the noise associated with the acceleration of the proof masses onboard each craft and the photon-shot noise. In general,

$$x^A(t) = n^A(t) + h^A(t) \quad , \quad (12)$$

where

$$h^A(t) = \sum_{i=1}^3 [p_i^A V_i^{\text{GW}}(t) + q_i^A U_i^{\text{GW}}(t)] \quad , \quad (13)$$

is the gravitational-wave strain in pseudo-detector A and $n^A(t)$ is the time-delayed sum of the remaining noise components. One typically assumes that these components and, hence, the total noise, has a Gaussian probability distribution with a zero mean. Their variance-covariance matrix elements are given as follows. For the photon-shot noise, these elements are

$$\begin{aligned} \overline{\tilde{n}_{U_i}^{\text{shot}*}(f) \tilde{n}_{U_j}^{\text{shot}}(f')} &= \overline{\tilde{n}_{V_i}^{\text{shot}*}(f) \tilde{n}_{V_j}^{\text{shot}}(f')} \\ &= \overline{\tilde{n}_{W_i}^{\text{shot}*}(f) \tilde{n}_{W_j}^{\text{shot}}(f')} = \frac{1}{2} P^{\text{shot}}(f) \delta(f - f') \delta_{ij} , \\ \overline{\tilde{n}_{U_i}^{\text{shot}*}(f) \tilde{n}_{V_j}^{\text{shot}}(f')} &= \overline{\tilde{n}_{V_i}^{\text{shot}*}(f) \tilde{n}_{W_j}^{\text{shot}}(f')} = \overline{\tilde{n}_{W_i}^{\text{shot}*}(f) \tilde{n}_{U_j}^{\text{shot}}(f')} = 0 \quad , \quad (14) \end{aligned}$$

for any i and j . Above, $P^{\text{shot}}(f)$ is termed as the one-sided power-spectral density (PSD) of the photon-shot noise. Furthermore, one assumes the proof-mass noise to be isotropic, such that:

$$\begin{aligned} \overline{(\hat{\mathbf{n}}_i \cdot \tilde{\mathbf{u}}_j^*(f)) (\hat{\mathbf{n}}_k \cdot \tilde{\mathbf{u}}_l(f'))} &= \overline{(\hat{\mathbf{n}}_i \cdot \tilde{\mathbf{u}}_{j^*}^*(f)) (\hat{\mathbf{n}}_k \cdot \tilde{\mathbf{u}}_{l^*}(f'))} = \frac{1}{2} P^{\text{proof}} \delta(f - f') \delta_{jl} , \\ \overline{(\hat{\mathbf{n}}_i \cdot \tilde{\mathbf{u}}_{j^*}^*(f)) (\hat{\mathbf{n}}_k \cdot \tilde{\mathbf{u}}_l(f'))} &= \overline{(\hat{\mathbf{n}}_i \cdot \tilde{\mathbf{u}}_j^*(f)) (\hat{\mathbf{n}}_k \cdot \tilde{\mathbf{u}}_{l^*}(f'))} = 0 , \end{aligned} \quad (15)$$

for any i, j, k , and l . Also, the covariance of the shot noise in any data stream with the noise in the motion of any proof-mass is zero. It is estimated that $P^{\text{shot}} = 1.8 \times 10^{-37} [f/1\text{Hz}]^2 \text{Hz}^{-1}$ and that the proof-mass noise PSD is $P^{\text{proof}} = 2.5 \times 10^{-48} [f/1\text{Hz}]^{-2} \text{Hz}^{-1}$. [3] While the proof-mass noise enters the very low frequency band of LISA, the shot noise enters the higher end of LISA's sensitivity band.

It is now possible to deduce the noise PSD, $P^{(A)}(f)$, of each of the pseudo-detectors from the above expressions. It follows from them that in the absence of a signal, each pseudo-detector is pure noise, $x^A(t) \equiv n^A(t)$, with a zero mean Gaussian probability distribution. The variance of this distribution is

$$\overline{\tilde{n}^{A*}(f) \tilde{n}^B(f')} = \frac{1}{2} P^{(A)}(f) \delta(f - f') \delta^{AB} . \quad (16)$$

By substituting for x^A from Eq. (7) (with U_i^{GW} and V_i^{GW} set to zero there) in the above equation and using the covariances of the noise components defined in Eqs (14) and (15) one finds [14]:

$$\begin{aligned} P^{(A)}(f) &= \sum_{i=1}^3 \left[(|2p_i^A + r_i^A|^2 + |2q_i^A + r_i^A|^2) P^{\text{proof}} \right. \\ &\quad \left. + (|2p_i^A|^2 + |2q_i^A|^2) P^{\text{shot}} \right] \end{aligned} \quad (17)$$

The resulting noise spectra for each pseudo-detector is [8]:

$$\begin{aligned} P^{(1)}(f) &= P^{(2)}(f) = 8 \sin^2(\pi f L) \{ [2 + \cos(2\pi f L)] P^{\text{shot}} \\ &\quad + [6 + 4 \cos(2\pi f L) + 2 \cos(4\pi f L)] P^{\text{proof}} \} , \\ P^{(3)}(f) &= [2 + 4 \cos(2\pi f L)] [P^{\text{shot}} + 4 \sin^2(\pi f L) P^{\text{proof}}] . \end{aligned} \quad (18)$$

Therefore, the data analysis challenge is to detect signals in this remaining noise.

3. The Signal

Since LISA will be orbiting the solar-system barycenter (SSB), it is convenient to introduce a reference frame centered at the SSB. As shown in Fig. 2, we define the $\hat{\mathbf{x}}$ and $\hat{\mathbf{y}}$ axes of this SSB frame to lie on the ecliptic, and the $\hat{\mathbf{z}}$ axis to be normal to it and pointing towards the north ecliptic pole. The $\hat{\mathbf{x}}$ axis points towards the vernal equinox. We take the GW source to be located in the direction given by the vector $\hat{\mathbf{w}}$. A gravitational wave from this source will arrive at the SSB origin traveling along $-\hat{\mathbf{w}}$. The sky position $\{\theta, \phi\}$ defines the Cartesian components of the propagation direction, i.e., $\hat{\mathbf{w}} = (\sin \theta \cos \phi, \sin \theta \sin \phi, \cos \theta)$. Thus, the sky-position angles are

equivalently characterized by two of the three components of $\hat{\mathbf{w}}$, say, $w_1 = \sin \theta \cos \phi$ and $w_2 = \sin \theta \sin \phi$. Also, θ_k and ϕ_k define the plane transverse to $\hat{\mathbf{w}}$:

$$\hat{\boldsymbol{\theta}} \equiv \frac{\partial \hat{\mathbf{w}}}{\partial \theta} \quad , \quad \hat{\boldsymbol{\phi}} \equiv \frac{1}{\sin \theta} \frac{\partial \hat{\mathbf{w}}}{\partial \phi} . \quad (19)$$

The perturbation created by the wave at a spacetime location (t, \mathbf{r}) is given by

$$h_{kl}(t, \mathbf{r}) = h_+(t - \hat{\mathbf{w}} \cdot \mathbf{r})(\theta_k \theta_l - \phi_k \phi_l) + h_\times(t - \hat{\mathbf{w}} \cdot \mathbf{r})(\theta_k \phi_k + \theta_l \phi_l) \quad , \quad (20)$$

where $h_+(t)$ and $h_\times(t)$ are the two GW polarizations and \mathbf{r} is the position vector of the spatial location of the perturbation in the SSB frame. In the time domain, the strain induced along the i th arm is

$$h_i(t) = h_{kl}(t) n_i^k n_i^l = h_{i+}(t) \xi_{i+}(w_1, w_2) + h_{i\times}(t) \xi_{i\times}(w_1, w_2) \quad , \quad (21)$$

where we used the Einstein summation convention over the repeated indices k and l . Above,

$$\xi_{i+} = (\hat{\boldsymbol{\theta}} \cdot \hat{\mathbf{n}}_i)^2 - (\hat{\boldsymbol{\phi}} \cdot \hat{\mathbf{n}}_i)^2 \quad , \quad \xi_{i\times} = 2(\hat{\boldsymbol{\theta}} \cdot \hat{\mathbf{n}}_i)(\hat{\boldsymbol{\phi}} \cdot \hat{\mathbf{n}}_i) \quad (22)$$

are the beam-pattern functions of the i th arm for the two polarizations.

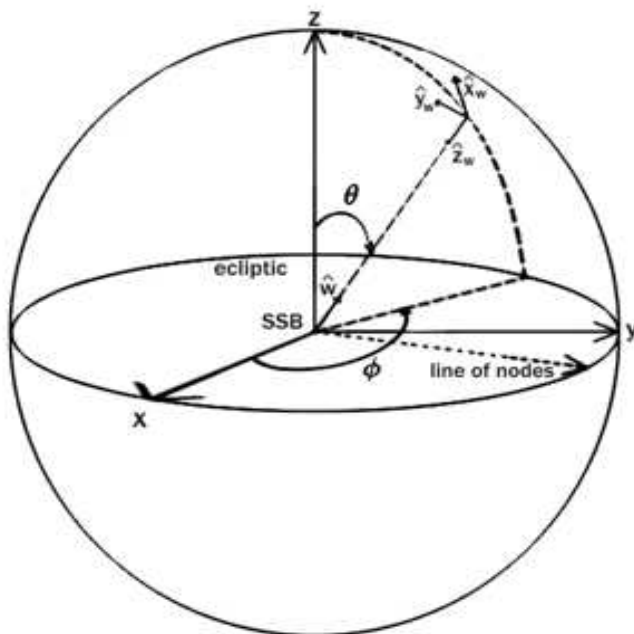


Figure 2. The solar-system barycentric (SSB) frame, denoted by the (x, y, z) axes. The angles (θ, ϕ) specify the sky position, $\hat{\mathbf{w}}$ of a GW source. The axes of the wave-frame associated with a gravitational wave emanating from that source are labeled by the unit-normal vectors $(\hat{\mathbf{x}}_w, \hat{\mathbf{y}}_w, \hat{\mathbf{z}}_w)$. The orientation of the wave frame relative to the SSB frame is given by the Euler angles, $(\phi - \pi/2, \pi - \theta, \psi)$, where ψ is the angle between the line of nodes and $\hat{\mathbf{x}}_w$ (as explicitized further on the left panel in Fig. 3). The celestial longitude is drawn as a dashed arc passing through the origin of the wave frame.

An impinging GW causes a change in the light-travel time along an arm that can be calculated by solving the null geodesic equation in the corresponding perturbed

spacetime. This in turn causes a time-varying Doppler shift, which clearly depends on the difference between the GW strains at the two space-crafts at the end of the arm. One also expects this shift to be dependent on the position of the source relative to the arm, $\hat{\mathbf{w}} \cdot \hat{\mathbf{n}}_i$. Thus, the GW contribution to the data stream V_i is given by [14]

$$V_i^{\text{GW}}(t) = \frac{-1}{2(1 - \hat{\mathbf{w}} \cdot \hat{\mathbf{n}}_i)} [h(t - \hat{\mathbf{w}} \cdot \mathbf{r}_{i+1}) - h(t - \hat{\mathbf{w}} \cdot \mathbf{r}_{i-1} - L)] \quad (23)$$

where \mathbf{r}_i is the position vector of the i th craft in the LISA frame.

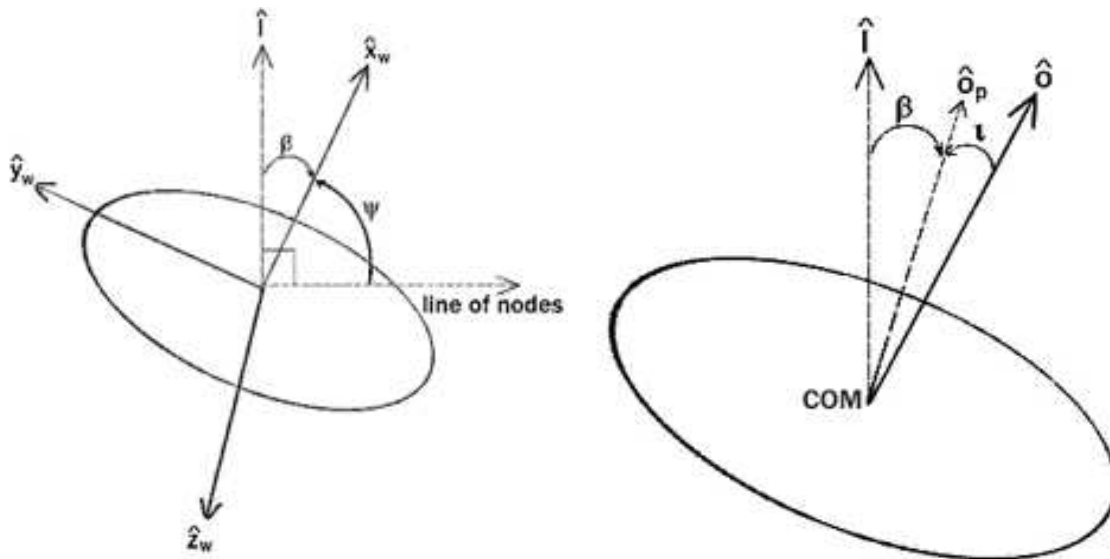


Figure 3. The left panel shows the wave frame and the right panel shows the orientation of the compact binary's orbit. The orientation of the wave frame is such that its $\hat{\mathbf{z}}_w$ axis points towards the origin of the SSB frame (as shown in Fig. 2) and its $\hat{\mathbf{x}}_w$ axis lies along the semi-major axis of the wave's polarization ellipse. The tangent, $\hat{\mathbf{l}}$, to the longitude at the source's sky-position is perpendicular to the line of nodes, which lies on the ecliptic. The two form a plane on which $\hat{\mathbf{x}}_w$ lies making an angle ψ with the line of nodes. Therefore, $\beta = \pi/2 - \psi$. In the right panel, COM is the center of mass of the binary. The normal, $\hat{\mathbf{o}}$, to its orbit is along the binary's orbital angular momentum vector and has an inclination of angle ϵ (introduced in the main text) with the line of sight, $\hat{\mathbf{w}}$. The projection of $\hat{\mathbf{o}}$ on the celestial sphere is $\hat{\mathbf{o}}_p$, which makes an angle β with respect to $\hat{\mathbf{l}}$. The angle between $\hat{\mathbf{o}}$ and $\hat{\mathbf{o}}_p$ is ι . These two angles, β and ι , completely specify the orientation of the orbit's normal. Thus, $\iota = \pi/2 - \epsilon$.

We now consider the effect of a signal from a non-spinning compact binary, with member masses m_1 and m_2 , on $V_i^{\text{GW}}(t)$. The two polarization amplitudes for the i th arm are

$$h_{i+}(t) = H(\Omega_i) \left[\frac{1 + \cos^2 \epsilon}{2} \cos 2\psi \cos(\Phi_i(t) + \delta_c) + \cos \epsilon \sin 2\psi \sin(\Phi_i(t) + \delta_c) \right] \quad (24)$$

$$h_{i\times}(t) = H(\Omega_i) \left[-\frac{1 + \cos^2 \epsilon}{2} \sin 2\psi \cos(\Phi_i(t) + \delta_c) + \cos \epsilon \cos 2\psi \sin(\Phi_i(t) + \delta_c) \right] \quad (25)$$

where $\Phi_i(t)$ is the phase received at that arm, $\{\psi, \epsilon\}$ are the polarization and inclination angles of the binary source (as explained in Fig. 3) and δ_c is the initial phase at the

origin of the LISA frame. For binaries that include a white-dwarf, the signal will be essentially monochromatic, with $\Phi_i(t) = \Omega_i t$. Above, $H(\Omega_i)$ is the signal amplitude at LISA defined as:

$$H(\Omega_i) = 1.188 \times 10^{-22} \left[\frac{\mathcal{M}}{1000 M_\odot} \right]^{5/3} \left[\frac{R}{1 \text{Gpc}} \right]^{-1} \left[\frac{\Omega_i}{2\pi \times 1 \text{mHz}} \right]^{2/3} \quad (26)$$

where $\mathcal{M} = (m_1 m_2)^{3/5} / (m_1 + m_2)^{1/5}$ is the chirp mass, R is the distance to the source and

$$\Omega_i = \Omega_0 \gamma_i \quad (27)$$

is the Doppler shifted source frequency, Ω_0 , at the i th arm owing to LISA's motion with respect to the solar-system barycenter. Note that γ_i is the sky-position dependent Doppler factor,

$$\gamma_i = (1 - \hat{\mathbf{w}} \cdot \hat{\boldsymbol{\eta}}_i) \quad , \quad (28)$$

where $\hat{\boldsymbol{\eta}}_i$ is the velocity of the geometrical center of the i th arm. Substituting the GW strain deduced from Eqs. (24) and (21) in the $V_i^{\text{GW}}(t)$ expression (23), manifests its dependence on the source parameters. One can similarly obtain $U_i^{\text{GW}}(t)$ as a function of these parameters. We first discuss the case of the monochromatic signal. The extension to slightly chirping sources is straightforward and will be presented subsequently.

If the laser-frequency and optical-bench motion noises were at the level of the other noises, one could hunt for GW signals in the U_i and V_i data streams. But as we saw in the last section, this is not the case and, hence, one has to search for them in the pseudo-detectors $x^A(t)$ in which the contributions of these noises stand canceled. Working with the $x^A(t)$, however, makes the data analysis formulation a little non-trivial since one has to contend with time-delaying appropriately the six inter-craft data streams that can potentially harbor a GW signal, $h^A(t)$. Implementing this is somewhat easier in the Fourier domain. Thus, the algorithm we follow in the rest of this section is as follows. We begin by first computing the Fourier transform of the data streams V_i^{GW} (and U_i^{GW}). These will then be time-delayed and combined to calculate the frequency components $\tilde{h}^A(\omega)$ (where $\omega = 2\pi f$) of the GW signal in the A th pseudo-detector, along the lines of Eq. (13). Its inverse Fourier transform will finally yield $h^A(t)$, which is the quantity we aim to search for in the $x^A(t)$. In the process, we get an explicit expression for $\tilde{h}^A(\omega)$, which is useful since the implementation of a search is faster in the Fourier domain, where one can avail of the existing Fast Fourier transform algorithms.[17]

We begin by defining two new functions of $\{\psi, \epsilon\}$ that appear naturally in the Fourier transforms, $\tilde{V}_i^{\text{GW}}(\omega)$ and $\tilde{U}_i^{\text{GW}}(\omega)$, of the six streams:

$$\begin{aligned} l_\times &= -i (T_2^2(\psi, \epsilon, 0) - T_2^{-2}(\psi, \epsilon, 0)) \quad , \\ l_+ &= (T_2^2(\psi, \epsilon, 0) + T_2^{-2}(\psi, \epsilon, 0)) \quad , \end{aligned} \quad (29)$$

where $T_2^{\pm 2}$ are Gel'fand functions [18],

$$T_2^{\pm 2}(\psi, \epsilon, 0) = \frac{1}{4} (1 \pm \cos \epsilon)^2 \exp(\mp i 2\psi) \quad . \quad (30)$$

To find $\tilde{V}_i^{\text{GW}}(\omega)$, we use the GW strain Eqs. (24) and (21) in the expression for $V_i^{\text{GW}}(t)$ in Eq. (23). Taking the Fourier transform of the result gives

$$\begin{aligned} \tilde{V}_i^{\text{GW}}(\omega) = H(\Omega_0)T \left[\right. & \text{sinc}((\omega - \Omega_i)T) e^{-i\delta_c} \times \\ & \left(l_+^*(\psi, \epsilon) F_{V_{i+1};+}^*(\Omega_i) + l_\times^*(\psi, \epsilon) F_{V_{i+1};\times}^*(\Omega_i) \right) \\ & + \text{sinc}((\omega + \Omega_i)T) e^{i\delta_c} \times \\ & \left. \left(l_+(\psi, \epsilon) F_{V_{i+1};+}(\Omega_i) + l_\times(\psi, \epsilon) F_{V_{i+1};\times}(\Omega_i) \right) \right]. \end{aligned} \quad (31)$$

The orientation of the i th arm resides in the functions,

$$\begin{aligned} F_{V_{i+1};+,\times} &= -ib_i \xi_{i;+,\times} \text{sinc}(\Omega_i L_i k_i^-) e^{i\tau_i \Omega_i L_i} \quad , \\ F_{U_{i-1};+,\times} &= ib_i \xi_{i;+,\times} \text{sinc}(\Omega_i L_i k_i^+) e^{i\tau_i \Omega_i L_i} \quad , \end{aligned} \quad (32)$$

where

$$b_i \equiv \frac{\Omega_0 \gamma_i^{5/3} L_i}{2}, \quad \tau_i \equiv \frac{1}{2} \left(1 - \frac{\hat{\mathbf{w}} \cdot \hat{\mathbf{r}}_i}{\sqrt{3}} \right), \quad k_i^\pm = \frac{(1 \pm \hat{\mathbf{w}} \cdot \hat{\mathbf{n}}_i)}{2} \quad , \quad (33)$$

are all real quantities. The $F_{U_{i-1};+,\times}$ similarly determine the fractional frequency shift \tilde{U}_i^{GW} . Note that the dependence on the angles $\{\psi, \epsilon\}$ has been separated out in the form of $l_{+,\times}$. We will exploit this separation of variables in the next section to eliminate the computational cost in searching over the $\{\psi, \epsilon\}$ angles for a GW signal.

The Fourier components of the GW strain $\tilde{h}^A(\omega)$ can now be found by combining the above $\tilde{V}_i^{\text{GW}}(\omega)$ (and $\tilde{U}_i^{\text{GW}}(\omega)$) via the Fourier analogue of Eq. (13). Thus,

$$\begin{aligned} \tilde{h}^A(\omega) = iH(\Omega_0)T \sum_i^3 \left[\right. & e^{-i(\delta_c + \sigma_i^A)} \text{sinc}((\omega - \Omega_i)T) T_2^{\rho*} D_{\rho i}^{A*} e^{-i\tau_i \Omega_i L_i} \\ & \left. + e^{i(\delta_c + \sigma_i^A)} \text{sinc}((\omega + \Omega_i)T) T_2^\rho D_{\rho i}^A e^{i\tau_i \Omega_i L_i} \right] \quad , \end{aligned} \quad (34)$$

where there is an implicit sum over $\rho = \pm 2$. Also, we define

$$D_{\pm 2j}^A \equiv b_j |M_j^A| (\xi_{j+} \mp i\xi_{j\times}) \quad , \quad (35)$$

where

$$M_i^A \equiv q_{i-1}^A \text{sinc}(\Omega_i L_i k_i^+) - p_{i+1}^A \text{sinc}(\Omega_i L_i k_i^-) \quad (36)$$

and $\sigma_i^A = \arg(M_i^A)$.

The time-domain expression of the GW strain in the pseudo-detector A is obtained by taking the Fourier transform of $\tilde{h}^A(\omega)$, and is found to be

$$h^A(t) = H(\Omega_0) \sum_{j=1}^3 \Re [e^{-i\delta} E_j^{A*} S_j(t)] \quad , \quad (37)$$

where $\delta = \delta_c + \pi/2$,

$$S_j^A(t) \equiv e^{i\Omega_j(t - L_j \tau_j) + i\sigma_j^A} / g_j^A \quad \text{and} \quad E_j^A \equiv g_j^A T_2^\rho D_{j\rho}^A \quad . \quad (38)$$

Above, g_j^A is a normalization constant such that

$$\langle S_j^A, S_j^A \rangle_{(A)} \equiv 4 \int_0^\infty df \frac{|\tilde{S}_j^A(f)|^2}{P^{(A)}(f)} = 1 \quad , \quad (39)$$

which implies that for an observation duration (i.e., signal integration time) T ,

$$g_j^A = \left[\frac{2T}{\pi P^{(A)}(\Omega_j)} \right]^{1/2} . \quad (40)$$

When considering a slightly chirping source (i.e., when $\dot{\Omega}_0 \ll \Omega_0/T$) one can expand the signal phase as

$$\Phi_i(t) = \Omega_i t + \frac{1}{2} \dot{\Omega}_i t^2 . \quad (41)$$

In that case, the only modification to $h^A(t)$ occurs in the S_i^A term:

$$S_j^A(t) = e^{i\Omega_j(t-L_j\tau_j)+i(\frac{1}{2}\dot{\Omega}_j t^2 + \sigma_j^A)} / g_j^A \quad , \quad (42)$$

which defines the time-domain template for chirping compact-object binaries. Note that apart from the normalization constant, the template $S_j^A(t)$ is a pure phase term. We will find this useful when deducing the matched filter in the following section.

Equations (27) and (28) show that $\dot{\Omega}_j$ is related to the sky position and the intrinsic chirp rate $\dot{\Omega}_0$. In order to ensure that the phase evolution of a template models that of a signal well, it is important to allow for non-zero $\dot{\Omega}_0$ in searches of binaries involving masses higher than those of white dwarfs, such as in searches of neutron-star binaries and binaries involving a neutron star and a black hole. This is because the gravitational radiation reaction on these sources is stronger than those involving white-dwarfs. The post¹-Newtonian waveform reveals that for small chirp masses and source frequencies, the waveform phase can be expanded as in Eq. (41), with

$$\dot{\Omega}_0 = \frac{48}{5} \left(\frac{\mathcal{M}}{2} \right)^{5/3} \Omega_0^{11/3} \quad , \quad (43)$$

Thus, determining $\dot{\Omega}_0$ is significant since, together with Ω_0 , it determines the binary chirp mass \mathcal{M} . And as shown by Eq. (26), additional knowledge of the amplitude will then help in estimating the distance to the binary.[19]

To summarize, the GW strain in pseudo-detector A is given by Eq. (34) and is determined by eight independent parameters, $\{R, \delta, \Omega_0, \dot{\Omega}_0, \psi, \epsilon, \theta, \phi\}$. To search for a signal we must devise a strategy to seek these strains for a range of parameter values accessible to LISA's pseudo-detectors. This is what we deal with in the next section.

4. The Optimal Statistic

Given three independent pseudo-detectors, x^A , we now ask what is the optimal detection statistic to look for GW signals, h^A , in them. In the absence of any prior probabilities and costs, the optimal detection strategy is the one that minimizes the rate of false dismissals for a given rate of false alarms. This is termed as the Neyman-Pearson

criterion. Under this criterion, and for zero-mean Gaussian noise, the detection statistic is the likelihood ratio, λ , defined as [20]

$$\ln \lambda = \sum_{A=1}^3 \left(\langle h^A, x^A \rangle_{(A)} - \frac{1}{2} \langle h^A, h^A \rangle_{(A)} \right) , \quad (44)$$

where the first term is the sum of the cross-correlations of the expected signal, h^A , with the respective data, x^A , over all pseudo-detectors. The cross-correlation for pseudo-detector A is given by

$$\langle h^A, x^A \rangle_{(A)} \equiv 4\Re \int_0^\infty df \frac{\tilde{h}^{A*}(f) \tilde{x}^A(f)}{P^{(A)}(f)} , \quad (45)$$

where $\Re(X)$ denotes the real part of a complex number X . The second term in Eq. (44) is an overall normalization that is independent of the data. Substituting for h^A from Eq. (37), we get:

$$\sum_{A=1}^3 \langle h^A, x^A \rangle_{(A)} = \sum_{A=1}^3 \sum_{i=1}^3 \Re [e^{-i\delta} E_i^{A*} C_i^A] , \quad (46)$$

where

$$C_i^A \equiv \langle S_i^A, x^A \rangle_{(A)} . \quad (47)$$

The double summation in Eq. (46) can be replaced with the single sum over a new index k ,

$$\sum_{A=1}^3 \sum_{i=1}^3 Y_i^A \equiv \sum_{k=1}^9 Y_{(k-1)\%3+1}^{\lceil \frac{k}{3} \rceil} , \quad (48)$$

where $A = \text{Ceiling}(k/3) = \lceil \frac{k}{3} \rceil$ and $i = \text{Mod}(k-1, 3) + 1 = (k-1)\%3+1$. [21] We simplify the above expressions further by consistently identifying $Y_{(k-1)\%3+1}^{\lceil \frac{k}{3} \rceil}$ with Y^k , which form the components of a 9-dimensional vector \mathbf{Y} . Thus, $Y^{k=1} \equiv Y_{i=1}^{A=1}$, $Y^{k=2} \equiv Y_{i=2}^{A=1}$, $Y^{k=3} \equiv Y_{i=3}^{A=1}$, $Y^{k=4} \equiv Y_{i=1}^{A=2}$, and so on. We use this algorithm to map the D_i^A , E_i^A , and C_i^A to the components, D^k , E^k , and C^k of 9-dimensional vectors \mathbf{D} , \mathbf{E} , and \mathbf{C} , respectively.

In the new notation, the cross-correlation statistic becomes

$$\sum_{A=1}^3 \langle h^A, x^A \rangle_{(A)} = \sum_{k=1}^9 \Re [e^{-i\delta} E_k^* C^k] = \Re [e^{-i\delta} \mathbf{E} \cdot \mathbf{C}] \quad (49)$$

and

$$\sum_{A=1}^3 \langle h^A, h^A \rangle_{(A)} = H^2(\Omega_0) \sum_{k=1}^9 E_k^* E^k \equiv H^2(\Omega_0) \|\mathbf{E}\|^2 \equiv \kappa^2 , \quad (50)$$

where $\|\mathbf{Y}\|$ denotes the norm of vector \mathbf{Y} . Therefore, κ^2 is a measure of the signal power accessible to LISA. It is usually less than the peak power $H^2(\Omega_0)$ owing to LISA's non-optimal orientation, \mathbf{E} , to a given source. The relative sensitivities of the three pseudo-detectors to different sky positions can now be studied by plotting the analogue

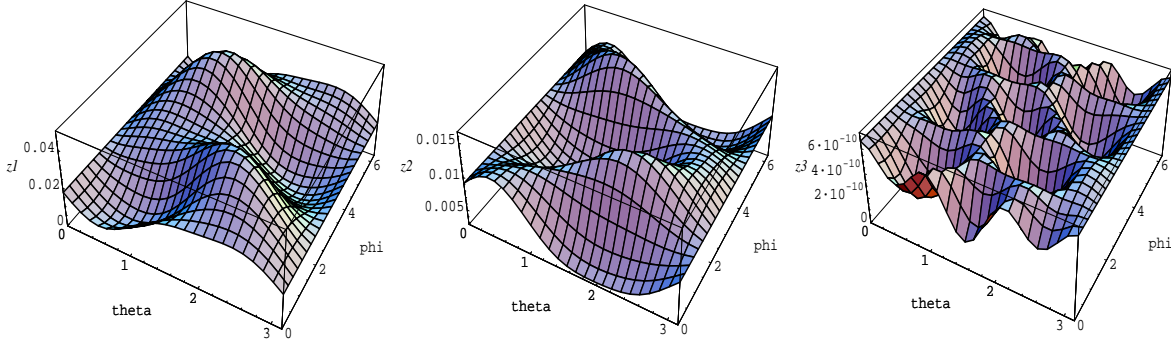


Figure 4. Sensitivities $z_A \equiv \sum_{i=1}^3 E_A^{i*} E_i^A / (g_i^A)^2$ of the three pseudo-detectors as functions of sky positions, $\{\theta, \phi\}$, in radians. Note that the Doppler shift in the source frequency has been ignored here; so g_i^A is the same for all i , i.e., $g_i^A \equiv g^A$. These plots have been evaluated for $\Omega_0 = 1$ mHz at the “initial” orbital position of LISA labeled $t = 0$. As illustrated above, direction of maximum sensitivity varies from one pseudo-detector to another.

of κ^2 for each individual pseudo-detector, as shown in Fig. 4. This figure, plotted for $\Omega_0 = 1$ mHz, verifies the fact found in Ref. [6] that the third pseudo-detector has a much smaller sensitivity than the first two. It also, shows that the *peak* sensitivity of the pseudo-detector labeled as $A = 1$ is the best of the three. However, at any given location on LISA’s orbit, there are sky positions to which pseudo-detector 2 has the best sensitivity. We also plot in Figs. 5 and 6, the sensitivities of pseudo-detector 1 and the optimal combination of all the pseudo-detectors, for three different locations on LISA’s orbit. These figures show that for all sky positions the optimal-sensitivity is better than the usually best pseudo-detector, labeled $A = 1$.

The likelihood ratio now takes the following form:

$$\ln \lambda = \kappa \sum_{A=1}^3 \langle \hat{h}^A, x^A \rangle_{(A)} - \frac{1}{2} \kappa^2, \quad (51)$$

where

$$\hat{h}^A \equiv \frac{h^A}{H(\Omega_0) \|\mathbf{E}\|} \quad (52)$$

is the normalized counterpart of h^A , such that $\sum_{A=1}^3 \langle \hat{h}^A, \hat{h}^A \rangle_{(A)} = 1$. The likelihood ratio can be maximized over κ and δ to yield

$$\ln \lambda |_{\hat{\kappa}, \hat{\delta}} = \frac{1}{2} |\mathbf{Q} \cdot \mathbf{C}|^2, \quad (53)$$

where the hat on a parameter denotes its value at which $\ln \lambda$ stands maximized with respect to that parameter and \mathbf{Q} is the normalized orientation vector, $\mathbf{Q} \equiv \mathbf{E} / \|\mathbf{E}\|$, such that $\|\mathbf{Q}\| = 1$. Also, we find $\hat{\kappa} = \sum_{A=1}^3 \langle \hat{h}^A, x^A \rangle_{(A)}$ and $\hat{\delta} = \arg(\mathbf{C} \cdot \mathbf{Q})$.

To maximize the statistic in Eq. (53) with respect to $\{\psi, \epsilon\}$, note that \mathbf{Q} can be expressed in terms of its components as follows:

$$\mathbf{Q} \equiv Q^{+2} \hat{\mathbf{D}}_{+2} + Q^{-2} \hat{\mathbf{D}}_{-2}, \quad (54)$$

where

$$\hat{\mathbf{D}}_{\pm 2} \equiv \frac{\mathbf{D}_{\pm}}{\|\mathbf{D}\|} \quad \text{and} \quad Q^{\pm 2} \equiv \frac{T_2^{\pm 2} \|\mathbf{D}\|}{\|\mathbf{E}\|}. \quad (55)$$

Above, we have used the fact that $\|\mathbf{D}_+\| = \|\mathbf{D}_-\| \equiv \|\mathbf{D}\|$. The statistic in Eq. (53) depends on $\{\psi, \epsilon\}$ solely through \mathbf{Q} . Therefore, it stands maximized with respect to those parameters when \mathbf{Q} gets aligned with \mathbf{C} . The fact that this alignment is physically realizable was shown in Ref. [23]. The maximized statistic is

$$\ln \lambda|_{\hat{\kappa}, \hat{\delta}, \hat{\psi}, \hat{\epsilon}} = \frac{1}{2} \|\mathbf{C}_{\mathcal{H}}\|^2, \quad (56)$$

where $\mathbf{C}_{\mathcal{H}}$ is the projection of \mathbf{C} on a 2-dimensional complex space, \mathcal{H} , spanned by $\{\hat{\mathbf{D}}_{+2}, \hat{\mathbf{D}}_{-2}\}$. Since it is always possible to choose a pair of real basis vectors to define this two-dimensional space, we take these vectors to be

$$\hat{\mathbf{o}}^{\pm} \equiv (\hat{\mathbf{d}}_1 \pm \hat{\mathbf{d}}_2) / \|\hat{\mathbf{d}}_1 \pm \hat{\mathbf{d}}_2\|, \quad (57)$$

where $\mathbf{d}_1 = \Re(\mathbf{D}_{+2})$ and $\mathbf{d}_2 = \Im(\mathbf{D}_{+2})$. Thus, we may define the network search statistic as

$$\Lambda \equiv \|\mathbf{C}_{\mathcal{H}}\|^2 = |C^+|^2 + |C^-|^2 = (c_0^+)^2 + (c_{\pi/2}^+)^2 + (c_0^-)^2 + (c_{\pi/2}^-)^2, \quad (58)$$

where $C^{\pm} = \hat{\mathbf{o}}^{\pm} \cdot \mathbf{C} \equiv c_0^{\pm} + ic_{\pi/2}^{\pm}$. The maximizing values of the two parameters are $\hat{\psi} = \arg(\varpi)/4$ and $\hat{\epsilon} = \cos^{-1} \left[(1 - \sqrt{|\varpi|}) / (1 + \sqrt{|\varpi|}) \right]$, where $\varpi \equiv C^{+2}/C^{-2}$.

The above statistic is still a function of the sky position through the parameters $\{w_1, w_2\}$. Since it is not possible to maximize the statistic over these parameters analytically, one must resort to a numerical maximization scheme as described in the following section. By comparing the values of the statistic for each pixel in the sky with a threshold value, Λ_0 , a decision on the presence or absence of a signal in the data can be made. The threshold itself is determined by the false-alarm probability that one can afford. Note that in the absence of a signal, Λ is a random variable that has a χ^2 probability distribution,

$$p_0(\Lambda) = \frac{\Lambda}{4} \exp(-\Lambda/2), \quad (59)$$

with 4 degrees of freedom [18]. This is because each of the c_0^{\pm} and $c_{\pi/2}^{\pm}$ is a Gaussian random variable with a zero mean and a unit variance. The false-alarm probability is

$$Q_0 = \int_{\Lambda_0}^{\infty} p_0(\Lambda) d(\Lambda) = \left(1 + \frac{\Lambda_0}{2}\right) \exp(-\Lambda_0/2). \quad (60)$$

In the presence of a signal, the probability distribution of Λ is non-central χ^2 ,

$$p_1(\Lambda) = \frac{\sqrt{\Lambda}}{2\kappa} \exp\left(-\frac{\Lambda + \kappa^2}{2}\right) I_1\left(\kappa\sqrt{\Lambda}\right), \quad (61)$$

with the non-centrality parameter as κ^2 , which is a measure of the signal power [18]. Above, I_1 is the modified Bessel function.

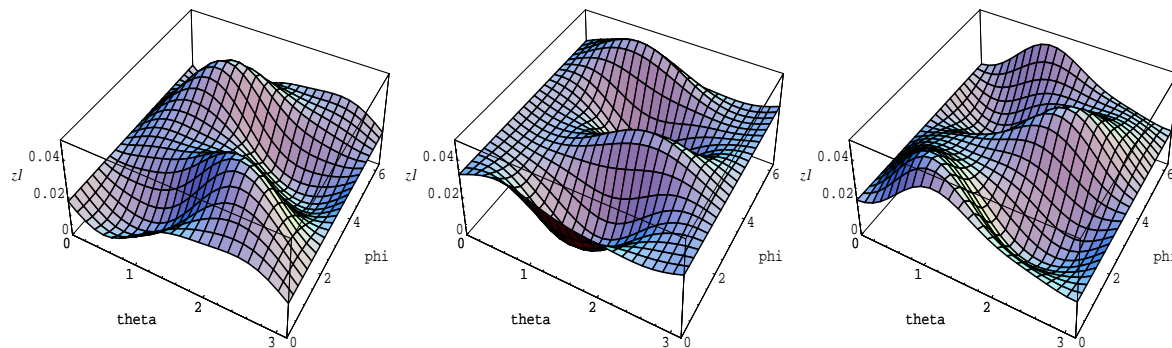


Figure 5. Sensitivity z_1 , as defined in Fig. 4, evaluated at $\Omega_0 = 1$ mHz for three different angular orbital positions (in radians), $\{0, \frac{\pi}{3}, \frac{2\pi}{3}\}$, with respect to the “initial” location denoted in Fig. 4. The left plot above is identical to the left plot in Fig. 4 since it corresponds to the same pseudo-detector and orbital location. Note that the sky positions corresponding to the sensitivity maxima vary from one location to another on LISA’s orbit.

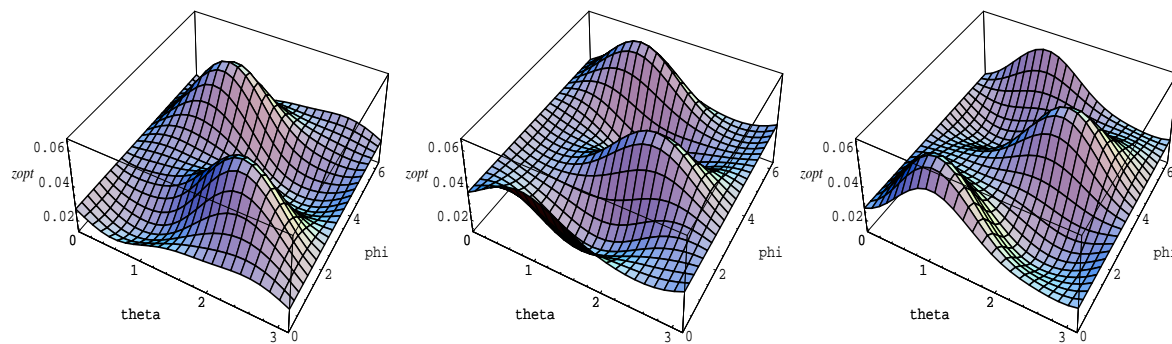


Figure 6. Network sensitivity $z_{opt} \equiv \sum_{k=1}^9 E_k^* E^k / (g^1)^2$ evaluated at $\Omega_0 = 1$ mHz for the same orbital positions that appear in Fig. 5. It is manifest that pseudo-detector 3 makes negligible contribution to the z_{opt} at this frequency. Note that $g^1 = g^2$. At any given sky position, the optimal statistic has better sensitivity than any z_A .

5. Template Spacing and Computational Costs

The Λ statistic in Eq. (56) must be maximized over the remaining intrinsic parameters, namely, $\boldsymbol{\vartheta} = \{\Omega_0, \dot{\Omega}_0, w_1, w_2\}$. As a first calculation, we will set $\dot{\Omega}_0 = 0$ and will focus on the number of templates required to scan the space of $\{\Omega_0, w_1, w_2\}$ for this case. As noted above, the ensuing template spacings will still be relevant to a large number of compact binaries that involve white-dwarfs. The corrections arising to these spacings for non-zero $\dot{\Omega}_0$ will be studied elsewhere. The maximization can then be achieved numerically using a discrete template bank over this three-dimensional parameter space. The drop in the value of the statistic and, therefore, the signal-to-noise ratio (SNR) that one can afford determines how coarsely one can space the templates. In practice, there are limits posed by the available computational resources on how fine the spacing can be. The

loss in SNR is related to the template spacing through the ambiguity function.[20]

The ambiguity function corresponding to the Λ statistic is derived from it by replacing the data x^A there by a signal $h^A(\boldsymbol{\vartheta}')$. We distinguish the signal parameter values from those of the template by denoting the former with a prime. The parameter values of a template used in a search may not be the same as those of a signal hiding in the data. Let the parameter mismatch be $\Delta\boldsymbol{\vartheta} \equiv (\boldsymbol{\vartheta}' - \boldsymbol{\vartheta})$. Then the ambiguity function is a real quantity expressed as

$$m(\boldsymbol{\vartheta}, \Delta\boldsymbol{\vartheta}) \equiv p_k^l Q'^k Q_l'^* \Theta_{(k)(l)}, \quad (62)$$

where Q'^k depends only on the signal parameters and

$$\begin{aligned} \Theta_{(k)(l)} &= \langle S'^k, S^k \rangle_{(k)}^* \langle S'^l, S^l \rangle_{(l)} \\ &= e^{i\Psi_k} e^{i\Psi_l} \text{sinc}(\Omega'_k T - \Omega_k T) \text{sinc}(\Omega'_l T - \Omega_l T), \end{aligned} \quad (63)$$

and $p_k^l \equiv o^{+l} o_k^+ + o^{-l} o_k^-$ is an amplitude factor. It is important to note that as $\Delta\boldsymbol{\vartheta} \rightarrow 0$, one has $m(\boldsymbol{\vartheta}, \Delta\boldsymbol{\vartheta}) \rightarrow 1$, which is the maximum value it can attain. The correlation phase, Ψ_k , is defined as

$$\Psi_k = L(\Omega'_k \tau'_k - \Omega_k \tau_k) = \Omega_k \frac{\hat{r}_{k1}}{2\sqrt{3}} \Delta w_1 + \Omega_k \frac{\hat{r}_{k2}}{2\sqrt{3}} \Delta w_2 - \tau_k \Delta \Omega_k. \quad (64)$$

The drop in the value of $m(\boldsymbol{\vartheta}, \Delta\boldsymbol{\vartheta})$ caused by non-zero, but small $\Delta\vartheta^\mu$, can be ascertained by Taylor expanding it about the maximum at $\Delta\boldsymbol{\vartheta} = 0$. [22, 23] The first order term is zero since by definition the statistic has a maximum when the template parameters match the signal parameters. Thus,

$$1 - m(\boldsymbol{\vartheta}, \Delta\boldsymbol{\vartheta}) \simeq \gamma_{\alpha\beta} \Delta\vartheta^\alpha \Delta\vartheta^\beta, \quad (65)$$

$\gamma_{\alpha\beta}$ is determined from the second order term in that expansion:

$$\gamma_{\alpha\beta} = -\frac{1}{2} \left(\frac{\partial^2 m(\boldsymbol{\vartheta}, \Delta\boldsymbol{\vartheta})}{\partial \Delta\vartheta^\alpha \partial \Delta\vartheta^\beta} \right) \Big|_{\Delta\boldsymbol{\vartheta}=0}. \quad (66)$$

It defines the metric on the 3-dimensional parameter space.

The computational cost for the search can be reduced by taking advantage of the Fast Fourier Transform algorithms [17] and computing the cross-correlation components, \mathbf{C} , in the Fourier domain. This defines the strategy for searching for the source frequency, Ω_0 . To search for the remaining parameters, $\{w_1, w_2\}$, one must design a bank of “templates” with values of these sky positions spaced such that the loss in SNR is never more than the desired fraction, say, μ . To find the metric, g_{ij} , on the two-dimensional space \mathcal{P} , spanned by $\{w_1, w_2\}$, we project $\gamma_{\alpha\beta}$ orthogonal to Ω_0 ,

$$g_{ij} = \gamma_{ij} - \frac{\gamma_{0i} \gamma_{0j}}{\gamma_{00}}, \quad (67)$$

where i and j span only the $\{w_1, w_2\}$ space, and the index 0 denotes the Ω_0 axis. The volume of a \mathcal{P} is then given by

$$\mathcal{V} = \int_{\mathcal{P}} \sqrt{\det \|g_{ab}\|} d^P \vartheta, \quad (68)$$

where $P = 2$ is the dimensionality of the space. The number density of templates, $\rho_P(\mu)$, is determined as a function of μ to be [23]:

$$\rho_P(\mu) = \left(\frac{1}{2} \sqrt{\frac{P}{\mu}} \right)^P. \quad (69)$$

Setting the fractional SNR loss $\mu = 3\%$ yields a template density of $\rho_2(0.03) = 16.6$. Therefore, the total number of templates is just the overall parameter volume times the template density, i.e., $N_{\text{templates}} = \mathcal{V} \times \rho_P(\mu)$.

The parameter volume, obtained via the metric computation, turns out to be about 5 for $\Omega_0 = 1$ mHz. Considering that the template density per unit volume is only 16.6 implies that the number of sky-position templates required for a search with 3% loss of SNR is about 80. The smallness of this number is not surprising, given how slowly the ambiguity function varies as a function of $\Delta\theta$ and $\Delta\phi$, as shown in Fig. 7.

As is manifest from Eq. (62), in principle, this variation can arise from either the time delays in Θ_{kl} or the weights p_k^l . However, for wavelengths much larger than the LISA arm length, the ability to discern between different sky positions through the time delays in Θ_{kl} is negligible. The main contribution to $m(\boldsymbol{\vartheta}, \Delta\boldsymbol{\vartheta})$, therefore, arises from the p_k^l . For detailed studies of the angular resolution achievable by LISA, we refer the reader to Refs. [24, 25].

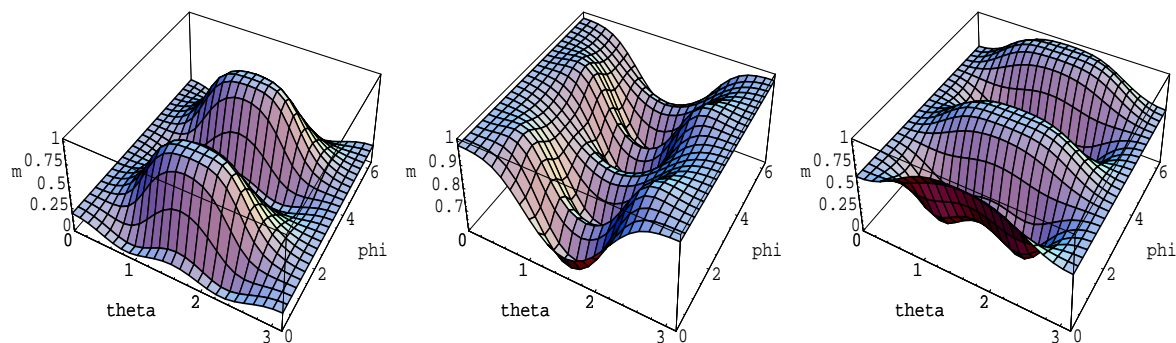


Figure 7. The ambiguity function m plotted as a function of the template parameters, $\{\theta, \phi\}$, for three different source sky positions (in radians), namely, $\{\theta', \phi'\} = \{\pi/2, 4\pi/3\}$, $\{\pi/6, \pi/3\}$, and $\{\pi/2, \pi\}$.

To get a handle on the computational costs associated with a search of this nature, one must determine the overall number of sampling points in a single data train. For our analysis, we have chosen a sampling rate of 1 Hz. Therefore, the number of sampling points is just the length of the data train, T . The number of floating point operations associated with an FFT with T sampling points is:

$$N_{\text{fl-opts}} = T \log_2 T. \quad (70)$$

Considering that this must be done for each template, the resulting expression for the total number of floating point operations for an arbitrary template bank is just

$N_{\text{templates}} \times N_{\text{ft-opts}}$. However, the real quantity of interest is the the number of operations per second,

$$C^{\text{flops}} \equiv \frac{N_{\text{templates}} \times N_{\text{ft-opts}}}{T} = N_{\text{templates}} \log_2 T. \quad (71)$$

Therefore, the computational costs of implementing a real-time search with about 80 templates on a year's worth of data is trivial since the number of flops scales logarithmically with the integration time.

6. Discussion

In this paper, we developed an optimal method for detecting slightly chirping compact-binary inspiral signals in the LISA data. We also studied the geometrical properties and sensitivities of the three noise-independent pseudo-detectors or data combinations of LISA. Following the earlier work on TDI data combinations, it was found [11, 12, 13] that the rotational motion of LISA and the time-variation of LISA's arm-lengths would prevent the noise contribution of the laser-frequency fluctuations from being mitigated to the level of the secondary noises. In order to tackle this problem, second generation pseudo-detectors were introduced as simple differences of their first generation counterparts, appropriately time-shifted:

$$x^{\bar{A}}(t) \equiv x^A(t) - x^A(t - L_1 - L_2 - L_3) \simeq x^A(t) - x^A(t - 3L). \quad (72)$$

The analysis presented above can be easily extended for detecting inspiral signals in the second generation pseudo-detectors, $x^{\bar{A}}(t)$, by implementing the next two steps: First, by following the derivation in Sec. 2 it can be verified that the noise PSDs of the new detectors are given in terms of the old ones by:

$$P^{(\bar{1}, \bar{2}, \bar{3})}(f) = 4 \sin^2(3\pi fL) P^{(1, 2, 3)}(f). \quad (73)$$

Second, since a GW contribution to $x^{\bar{A}}(t)$ will also get differenced as in Eq. (72), the template that must be matched against $x^{\bar{A}}(t)$ should itself be modified accordingly:

$$S_i^{\bar{A}}(t) \equiv S_i^A(t) - S_i^A(t - L_1 - L_2 - L_3) \simeq S_i^A(t) - S_i^A(t - 3L). \quad (74)$$

None of the formal analysis presented in this paper is affected by this change. For example, the analytic maximization of the likelihood ratio over four source parameters (namely, the signal strength, the initial phase, the polarization angle and the orbital-inclination angle), and the concomitant computational gain achieved in the process, still hold so long as the matched-filter output in Eq. (47) is redefined to be

$$C_i^{\bar{A}} = \langle S_i^{\bar{A}}, x^{\bar{A}} \rangle_{(\bar{A})}. \quad (75)$$

Also, the sensitivity plots in Figs. 4, 5, and 6 for the first generation detector A are the same as those of its second generation counterpart, i.e., detector \bar{A} . This is because the (geometric) sensitivity, z_A , depends on the orientation of a detector relative to the source and is independent of the noise PSDs. Similarly, the formal expressions for the ambiguity function in the last section above remain unchanged. But, since this function

depends on the noise PSDs, its numerical value is affected by the change in Eq. (73). Nevertheless, we have found that this change has negligible effect on the number of templates deduced in Sec. 5.

A useful by-product of our analysis is that it yields the maximum-likelihood estimates of the initial phase, the polarization angle, and the angle of inclination (in addition to, of course, the signal amplitude). To complete the parameter estimation problem, however, one needs to derive the errors associated with them as well as in the parameters that will be searched for numerically, viz., $\{\Omega_0, \dot{\Omega}_0, \theta, \phi\}$. That problem will be addressed elsewhere.

Acknowledgments

We would like to thank Rajesh Nayak for helpful correspondence. We are grateful to Massimo Tinto for pointing out to us that in the long-wavelength approximation, the contribution from the GW strain to third pseudo-detector discussed here should become negligible. The pseudo-detector sensitivities plotted in Fig. 4 verify this claim. We would also like to thank Curt Cutler for critically reading the manuscript and apprising us of Ref. [10], which is a closely related work on the data analysis of gravitational-wave signals from spinning neutron stars for Earth-based laser interferometric detectors. This work was funded in part NASA Grant NAG5-12837.

- [1] R. A. Hulse and J. H. Taylor, *Astrophys. J.* **195**, L51 (1975).
- [2] J. H. Taylor, L. A. Fowler and P. M. McCulloch, *Nature* **227**, 437 (1979).
- [3] “LISA: A Cornerstone Mission for the Observation of Gravitational Waves,” System and Technology Study Report, 2000.
- [4] J. W. Armstrong, F. B. Estabrook, and M. Tinto, *Astrophys. J.*, **527**, 814 (1999).
- [5] P. C. Peters, *Phys. Rev.* **136**, B1224 (1964).
- [6] A. Prince, M. Tinto, L. Larson and W. Armstrong, *Phys. Rev. D* **66**, 122002 (2002) [arXiv:gr-qc/0209039].
- [7] M. Tinto and J. W. Armstrong, *Phys. Rev. D* **59**, 102003 (1999).
- [8] A. Krolak, M. Tinto and M. Vallisneri, “Optimal filtering of the LISA data,” [arXiv:gr-qc/0401108].
- [9] A similar statistic has been obtained independently by Krolak *et. al.* recently [8]. Their method of analytically maximizing over four source parameters is similar to a method found in Ref. [10] for spinning neutron stars, and is manifestly different from ours. Furthermore, in our statistic we have retained the effect of the Doppler shift in the source emission frequency. When this effect is dropped, our (likelihood ratio) statistic is the same as in Ref. [8].
- [10] P. Jaranowski, A. Krolak and B. F. Schutz, *Phys. Rev. D* **58**, 063001 (1998) [arXiv:gr-qc/9804014].
- [11] N. J. Cornish and R. W. Hellings, *Class. Quant. Grav.* **20**, 4851 (2003) [arXiv:gr-qc/0306096].
- [12] D. A. Shaddock, M. Tinto, F. B. Estabrook and J. W. Armstrong, *Phys. Rev. D* **68**, 061303 (2003) [arXiv:gr-qc/0307080].
- [13] M. Tinto, F. B. Estabrook and J. W. Armstrong, *Phys. Rev. D* **69**, 082001 (2004) [arXiv:gr-qc/0310017].
- [14] S. V. Dhurandhar, K. Rajesh Nayak and J. Y. Vinet, *Phys. Rev. D* **65**, 102002 (2002) [arXiv:gr-qc/0112059].
- [15] K. R. Nayak, S. V. Dhurandhar, A. Pai and J. Y. Vinet, *Phys. Rev. D* **68**, 122001 (2003) [arXiv:gr-qc/0306050].
- [16] K. R. Nayak, A. Pai, S. V. Dhurandhar and J. Y. Vinet, *Class. Quant. Grav.* **20**, 1217 (2003) [arXiv:gr-qc/0210014].

- [17] For an explanation on what the FFT algorithms are and how they work see, e.g.: W. H. Press, S. A. Teukolsky, W. T. Vetterling, and B. P. Flannery, “Numerical Recipes in C,” (Cambridge University Press, second edition, 1993)
- [18] A. Pai, S. Dhurandhar and S. Bose, Phys. Rev. D **64**, 042004 (2001) [arXiv:gr-qc/0009078].
- [19] B. F.Schutz, Nature **323**, 310 (1986).
- [20] C. W. Helstrom, *Statistical Theory of Signal Detection* (Pergamon Press, London, 1968).
- [21] Although widely used by programmers, the operations of Ceiling and Modulus may not be familiar to most physicists and astronomers. The Ceiling of x is denoted as $\lceil x \rceil$ and is equal to the smaller integer not less than x . E.g., for $k = 2$, the Ceiling($k/3$) equals 1; and for $k = 6$, it is 2. On the other hand, x modulus y is expressed as $x\%y$ and is equal to the remainder when x is divided by y . E.g., $2\%3 = 2$ and $6\%3=0$.
- [22] B. J. Owen, Phys. Rev. D **53**, 6749 (1996). (gr-qc/9511032)
- [23] S. Bose, A. Pai and S. V. Dhurandhar, Int. J. Mod. Phys. D **9**, 325 (2000) [arXiv:gr-qc/0002010].
- [24] C. Cutler, Phys. Rev. D **57**, 7089 (1998).
- [25] R. Takahashi and N. Seto, Astrophy. J. **575**, 1030 (2002).